Exploring Shear-free Ringlet Formation with Direct Simulations of Saturn's B Rings

Yuxi Lu[1] , Ronald-Louis Ballouz[1,2] , and Derek C. Richardson[1]
[1] University of Maryland, College Park, MD 20742, USA
[2] Institute of Space and Astronautical Science, Japanese Aerospace Exploration Agency, Sagamihara, Kanagawa Prefecture, 252-5210, Japan

Abstract

In this paper, we study the effect of interparticle cohesion in numerical simulations of Saturn's main rings. Theoretical studies propose that the irregular structure in Saturn's rings may arise from alternating "solid" and "liquid" ring material. These studies suggest that for sufficiently high interparticle cohesion, shear-free rings around Saturn may form. We use a highly optimized *N*-body code that models particle self-gravity, soft-sphere collisions, and interparticle cohesion to simulate a patch of Saturn's rings with periodic boundaries. We present results for nine different cohesion values ranging from 5.0×10^{-2} to $7.0 \, \mathrm{Pa}$, dynamical optical depths of 0.8, 1.4, and 1.8, particle material densities of 0.5 and $1 \, \mathrm{g \, cm^{-3}}$, and restitution coefficients of 0.8 and 0.55. Our simulations show a transition of ring particles forming self-gravity wakes to forming structureless uniform distributions of smaller and faster-moving clumps as cohesion increases. The transition from wakes to structureless form occurs at lower inner-particle cohesion values for higher dynamical optical depth. We present an analysis of the physical optical depth, particle number density, and structure characteristics in the simulations at equilibrium. For high cohesion values, energy injection from differential shear causes transient large structures to rotate and collide at high speed, breaking them apart, ultimately limiting the clump size and frustrating the formation of shear-free zones.

Key words: planets and satellites: dynamical evolution and stability – planets and satellites: rings

1. Introduction

As the *Voyager* 1 and 2 spacecraft flew by the Saturnian system, they revealed the intricacies of its rings, showing rich radial structures surrounding the gas giant. More than two decades later, detailed observations from the *Cassini* spacecraft showed that this structure exists on many different scales, from hundreds of kilometers down to hundreds of meters (Porco et al. 2005; Colwell et al. 2007, 2009). The A and B rings, in particular, exhibit complexity as uncovered by photometric optical depth measurements (Colwell et al. 2009). While some of the large-scale structure in the A ring can be explained from density or bending waves generated by discrete resonances with inner satellites, the physical mechanism that produces most of the radial structure, particularly the smaller-scale structure, still remains a mystery.

Various mechanisms have been proposed to explain the irregular structure in Saturn's main rings. Salo (1992) showed that the self-gravity of the ring particles can form 100 m scale transient structures. These self-gravity wakes are chiefly characterized by their pitch angle of 10°–30°, the angle that the opaque clumps form with respect to the azimuthal (orbital) direction of motion. If the ring particles collide frequently and dissipate enough energy, then axisymmetric structure can develop. These structures develop through a viscous overstability (Salo et al. 2001), which forces local overdense regions of particles to periodically develop and dissipate in timescales of a few times per orbital period, depending on particle properties. *Cassini* has observed various features predicted by these two mechanisms. Observations of stellar occultations using the Visual and Infrared Mapping Spectrometer by Hedman et al. (2014) revealed that regions of large axisymmetric structure exist in the A-Ring, hinting at a viscous overstability mechanism at play in that region of Saturn's ring.

Numerous theoretical analyses have studied these two mechanisms (self-gravity wakes and viscous overstability) in detail through methods that either simulate the individual particle interactions in a local patch of the ring (Salo et al. 2001; Rein & Latter 2013; Ballouz et al. 2017) or through hydrodynamic modeling of a fluid disk to study the long-term stability of the system (Schmidt et al. 2001; Lehmann et al. 2017). However, these studies ignored the effect of interparticle cohesion on the short- and long-term evolution of the disk.

Before *Cassini*'s arrival to Saturn, Tremaine (2003) introduced an alternative mechanism to explain the large-scale structures seen in *Voyager* images. They proposed that the cohesive forces between ring particles could "freeze" them together creating alternating annuli of shear-free "solid" and shearing "liquid" ring material. The solid rings would be frozen into rigid rotation around Saturn, while the liquid material consisting of individual particles experiencing differential rotation. The size of the solid rings would be limited by the competition between tidal forces and the tensile strength of these assemblies that arises out of the collective effect of the individually weak interparticle cohesive forces. Tremaine (2003) showed that if shear stress is a decreasing function of the shear in the ring, then the ring is unstable at short wavelengths, and can form shear-free ringlets. While *Cassini*'s arrival at Saturn revealed that collisional and gravitational forces dominate smaller-scale structure in Saturns opaque rings, the active role of interparticle cohesion in affecting structure formation is still poorly understood, and may still effect the dynamics and observable properties in different parts of the ring.

Laboratory experiments have shown that the icy particles of Saturn would likely experience some cohesion. Experiments of collisions between frost-covered icy spheres (Bridges et al. 1984) show that these bodies can adhere at low impact speeds. Some groups have modeled the effect of cohesion between a small number of bodies (e.g., Spahn et al. 2004).

Albers & Spahn (2006) included cohesive forces between elastic solids in contact (Johnson et al. 1971) in the visco-elastic model (Brilliantov et al. 1996). Perrine et al. (2011) introduced a new method to model cohesion in planetary rings through a particle aggregation model that creates nondeformable but breakable structures. Their work was a first-order investigation of how semi-rigid bonding affects the evolution of particle assemblies in high-density environments. This cohesion model was used in Perrine & Richardson (2012) to study how bond parameters affect the size and size distribution of particle aggregates. While the cohesion model they used was simple, they were able to reproduce particle size and size distributions in Saturn's opaque A and B rings for ring-particle merge thresholds that match laboratory experiments (Hatzes et al. 1991).

Recent work analyzing the stability of small solar system bodies that are spun up by solar radiation pressure has revitalized the study of cohesive forces and its effect on the structure of gravitational aggregates in the solar system (Sánchez & Scheeres 2014; Zhang et al. 2018). Scheeres et al. (2010) analyzed a number of physical effects that act on particles on asteroid surfaces and found that van der Waals cohesive forces can be comparable or even exceed the strength of gravity in small bodies. Critically, the relative importance of cohesion is a function of the grain size, which is well constrained in Saturn's opaque rings. For example, UVIS occultation data placed a lower limit of 1 mm for the minimum grain size in Saturn's A ring (Becker et al. 2016). However, due to the weak self-gravity of subkilometer size structure, the relative strength of cohesion for grains as large as a few millimeters can begin to dominate the dynamics of the system, even for conservative values of cohesive strength (∼a few Pa).

In this study, we perform direct numerical simulations of a patch of particles in Saturn's A and B rings and include the effect of interparticle cohesion. Our N-body code allows us to study the collisional and gravitational dynamics in high-optical-depth regions of Saturn's rings. Using a recently implemented particle friction model that allows us to better model long-lasting static contacts (Zhang et al. 2017) and an interparticle cohesion model (Zhang et al. 2018), we analyze how interparticle cohesion affects structure formation and what role cohesion has in the evolution of Saturn's dense rings.

In Section 2, we describe the numerical method used in this work to simulate ring particle dynamics (the combined effect of self-gravity, collisions, and interparticle cohesion) and the analysis toolbox we have developed to study the formation of large structures in a ring patch. In Section 3, we present the simulation results showing the effects of increasing interparticle cohesion on structure formation in ring patches with properties similar to that of the A- and B-rings. In Section 4, we discuss these results, and in Section 5 we present conclusions and suggestions for further study.

2. Methodology

Building on the work described in Ballouz et al. (2017), we perform numerical simulations of a patch of ring particles using the code `pkdgrav` (Richardson et al. 2000; Stadel 2001) with a soft-sphere collision model (Schwartz et al. 2012). This paper presents an improvement on the functionality of `pkdgrav` presented in Ballouz et al. (2017) through the inclusion of a more appropriate particle shape-factor model for governing soft-sphere collisions (Zhang et al. 2017) and a newly implemented

interparticle cohesion model (Zhang et al. 2018). `pkdgrav` uses a parallelized tree code to speed up the calculation of the particles' mutual self-gravity. A second-order leapfrog method is used to integrate the equations of motion, with accelerations due to gravity and contact forces recomputed each step.

2.1. Numerical Method: Equations of Motion and Collisional Code

Following Wisdom & Tremaine (1988; also see Perrine et al. 2011; Ballouz et al. 2017), we perform local simulations of ring particles in a comoving patch frame. The equations of motion are solved in the Hill approximation, a corotating local coordinate system (Hill 1878). The equations of motion for a test particle are given by

$$\ddot{x} = F_x + 3\Omega^2 x + 2\Omega\dot{y}, \tag{1}$$

$$\ddot{y} = F_y - 2\Omega\dot{x}, \tag{2}$$

$$\ddot{z} = F_z - \Omega^2 z, \tag{3}$$

where $\boldsymbol{F} = (F_x, F_y, F_z)$ is the acceleration due to particle self-gravity and contact forces, x, y, and z are the coordinates of the particle in the local coordinate system (whose origin is located at the center of the patch; positive x is in the radial direction away from Saturn, positive y is in the orbital direction, and positive z points out of the ring plane according to the right-hand rule), and the derivatives are with respect to time. These equations of motion allow us to use shear-periodic boundary conditions in the plane of the patch.

The collisional component of `pkdgrav` incorporates a soft-sphere discrete element method (SSDEM; Schwartz et al. 2012). In SSDEM, spherical particles are allowed to overlap slightly, which is meant to represent deformation at the point of contact. Particle contacts can last many time steps, with reaction forces dependent on the degree of overlap and contact history. By allowing particles to overlap, multicontact and frictional forces can be modeled. Our implementation of SSDEM uses a spring/dashpot mechanism for the contact forces. In this model, two overlapping particles will apply a normal contact force, $\boldsymbol{F}_N$, and a tangential stick-slip force, $\boldsymbol{F}_T$. In the current implementation, contact forces are determined by restoring forces with optional damping and/or friction (static, rolling, and/or twisting):

$$\boldsymbol{F}_N = -k_N x\hat{\boldsymbol{n}} + C_N \boldsymbol{u}_N,$$
$$\boldsymbol{F}_T = \min(k_T \boldsymbol{\delta}_T + C_T \boldsymbol{u}_T, \mu_S|\boldsymbol{F}_N|\boldsymbol{\delta}_T/|\boldsymbol{\delta}_T|), \tag{4}$$

where k_N and k_T are the normal and tangential spring constants, respectively. Here the min() function indicates taking the vector quantity of smallest magnitude. The damping parameters (C_N, C_T) are related to the conventional normal and tangential coefficients of restitution used in hard-sphere implementations, ε_n and ε_t (see Schwartz et al. 2012 for further details). x is the mutual overlap of the two particles in length units, $\boldsymbol{\delta}_T$ is the sliding displacement from the equilibrium contact point, and $\hat{\boldsymbol{n}}$ is the unit vector from the particle's center to its neighbor. $\boldsymbol{u}_N$ and $\boldsymbol{u}_T$ are the normal and tangential components of the total relative velocity between the two particles at the point of contact, respectively. The coefficient of static friction, μ_s, determines the maximum amount of tangential force that can be supported by the contact point.

Twisting resistance arises from the slip and friction at the contact region due to a difference in the rotation rate of the

particles in a direction along the normal vector $\hat{\boldsymbol{n}}$. Rolling resistance can come about from a number of sources including slip and friction on the contact surface and shape effects. Both resistances are modeled as functions of the relative twisting or rotational angular velocity that can reach critical values based on a shape parameter, β, after which they maintain a maximum resisting torque (see Section 2.2 of Zhang et al. 2017). β represents a statistical measure of real particle shape, which has been found to be one of the primary physical mechanisms for rotational resistance that also plays an important role in modeling interparticle cohesion. See Zhang et al. (2017) for the full equations describing the torque contributions to the contact forces.

Previous studies (Iwashita & Oda 1998; Mohamed & Gutierrez 2010) have shown that the inclusion of rotational resistances into a contact model allows numerical simulations to better match laboratory experiments. Our previous study (Ballouz et al. 2017) showed that rolling friction is an important micro-scale feature that can control whether kilometer-scale self-gravity wakes or vertically coherent viscous overstability structure develops in the ring. In that study, we used a rotational resistance implementation (Schwartz et al. 2012) that is suited for the modeling of the dynamic flow of granular material. For this work, we anticipate that the development of shear-free zones in our simulations may be better modeled with a rotational resistance implementation developed in Zhang et al. (2017) that is better suited for grains in a quasi-static state. This is because the new method uses a spring-dashpot model for rolling resistance that keeps track of the original point of contact and is able to account for static rolling friction, which is more appropriate for dense particle systems. There are some models that can accurately capture the rotational resistance properties of grains in a mixture of the two states (dynamic flow and quasi-static aggregates, Ai et al. 2011); however, a full-scale comparison of rotational resistance models is beyond the scope of this work.

In the quasi-static-state implementation we use here, two rotational resistances are modeled: twisting and rolling resistance (parameterized through the friction coefficients μ_R and μ_T). The SSDEM implementation of pkdgrav has been validated through comparison with laboratory experiments (Schwartz et al. 2014) and has been used for various solar system applications: size-sorting on asteroids (Maurel et al. 2017), avalanche dynamics (Yu et al. 2014), the stability of asteroid rotations (Zhang et al. 2017, 2018), and collisions between rubble piles at low speeds (Ballouz et al. 2014, 2015).

2.2. Cohesion Model

In this paper, we introduce the use of an interparticle cohesive force between particles in a ring-patch simulation due to Zhang et al. (2018), who applied it to the study of critical spin limits of asteroids. The cohesive forces between ring particles may arise from van der Waals forces due to molecular or atomic polarization effects between micro-sized particles (Scheeres et al. 2010). Zhang et al. (2018) implemented a cohesion model in pkdgrav based on hypothetical contact between microscopic grains characterized by the shape parameter β (introduced in the end of Section 2.1). In this model, β represents a statistical measure of the area where the interstitial grains are in contact. The effective contact area, A_{eff},

between two grains is given by

$$A_{\mathrm{eff}} = 4(\beta R)^2, \tag{5}$$

where R is the effective particle radius, $R = R_p R_n / (R_p + R_n)$, and R_p and R_n are the radii of the particle and its neighbor, respectively. The cohesive contact force, $\boldsymbol{F}_C$, between the two particles is given by

$$\boldsymbol{F}_C = c A_{\mathrm{eff}} \hat{\boldsymbol{n}}, \tag{6}$$

where c is the interparticle cohesive tensile strength. The value of c reflects the physical properties of the interstitial microscopic grains: porosity, size distribution, surface energy, etc. The two particles only feel a cohesive force when they are in contact.

The value of the cohesive tensile strength for planetary ring particles is not well constrained in the literature. As a result, we tested a wide range of cohesion values in order to see its effect. For this study, after experimenting with cohesion coefficient values (c) from 0 to 10 Pa, we settled on the range 5×10^{-2} to 7 Pa, as smaller values were indistinguishable from using zero and larger values resulted in coherent structures on the order of the patch size, which invalidate the sliding patch model constraints. Note that this range is consistent with the values of a few to 100 dyn found by Hatzes et al. (1991) in their ice ball experiments.

2.3. Patch and Particle Properties

For the simulations presented in this paper, we set $k_t = \frac{2}{7} k_n$ in Equation (4) to keep the damped harmonic frequencies of the normal and tangential springs in phase—see Schwartz et al. (2012). An appropriate value of k_n is given by

$$k_n \sim m \left(\frac{v_{\mathrm{max}}}{x_{\mathrm{max}}} \right)^2, \tag{7}$$

where m is the mass of a typical energetic particle, v_{max} is the maximum expected relative particle speed in the simulation, and x_{max} is the maximum allowed particle overlap, which we set to be $\sim 1\%$ of the smallest particle radius. The timestep is set so that a typical collision (i.e., a full oscillation of the normal spring) takes about 30 steps. The typical collision speeds, v_{coll}, in a shearing patch frame are given by the Keplerian orbital frequency, Ω, and the typical radius, R_{particle}, of the ring particles:

$$v_{\mathrm{coll}} \sim \Omega R_{\mathrm{particle}}. \tag{8}$$

In order to be conservative with our estimation of typical collision speeds, we set v_{max} to be an order of magnitude larger than v_{coll}. For a ring patch at a Keplerian orbit 100,000 km from Saturn (B Ring) and ring particles with $R_{\mathrm{particle}} = 1$ m, we use $k_n = 4.2 \times 10^3$ kg s^{-2}, and a timestep of 0.074 s.

The friction properties of ring particles can influence the types of structures that are able to develop in opaque ring patches (Ballouz et al. 2017); however, they are poorly constrained. Here, we use a set of parameters, $\mu_s = 1.0$, $\mu_R = 1.05$, $\mu_T = 1.3$, $\beta = 0.5$, as nominal values of the friction coefficients in order to mimic the interaction of sand particles of medium hardness that have an angle of repose of $\sim 30°$ (Jiang et al. 2015; Zhang et al. 2017).

We simulate patches located in the B ring of dynamical optical depths of 0.8, 1.4, and 1.8 and surface densities between
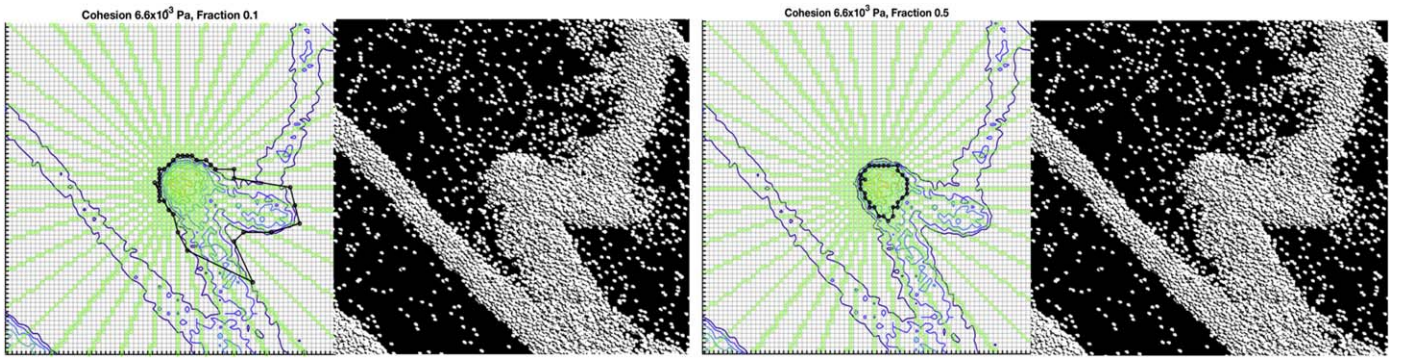
Figure 1. Analysis from the clump-finding algorithm using a threshold of 0.1 (left) and a threshold of 0.5 (right) for a dynamical optical depth value of 0.8, particle density of 1 g cm^{-3}, and cohesion value of 6.6×10^{-3} Pa. The green lines with circle markers are the branches crossing the maximum particle number density, the blue lines are the density contours, and the black lines define the aggregates identified by the algorithm. On the right of each plot is a snapshot of the corresponding region of the simulation.

Table 1
Ring and Patch Properties Used in the Presented Simulations

Parameter	Values/Range
Bulk Density (g cm^{-3}) (ρ)	0.5, 1.0
Cohesive Strength (Pa) (c)	5×10^{-2} to 7.0
Number of Particles	$\sim$22,000 to $\sim$250,000
Dynamic Optical Depth (τ_D)	0.8, 1.4, 1.8
Restitution ($\varepsilon_N//\varepsilon_T$)	0.8, 0.55

530 and 2400 kg m^{-2}. The dynamical optical depth $\tau_{\rm dyn}$ of a ring is defined as

$$\tau_{\rm dyn} = \int \pi R_{\rm particle}^2 n(R_{\rm particle}) {\rm d}R_{\rm particle}, \qquad (9)$$

where $R_{\rm particle}$ is the particle radius and $n(R_{\rm particle})$ is the surface number density of ring particles whose sizes are between $R_{\rm particle}$ and $R_{\rm particle} + dR_{\rm particle}$. For equal-size particles, this reduces to $\tau_{\rm dyn} = N\pi R_{\rm particle}^2/S$, where N is the number of particles and S is the area of the patch. We consider the middle optical depth value to be nominal in our simulations as it is typical of the B ring, and it corresponds to a number of particles that can be feasibly simulated in a timely fashion using our code.

The values of the patch surface density in our simulations cover the range found in Saturn's B ring (400–1400 kg m^{-2}; Hedman & Nicholson 2016). In order to ensure that we allow sufficient space for the formation of large-scale structures, we simulate a patch that is at least 4 λ_{cr} in the radial direction and 4 λ_c in the azimuthal direction, where λ_c is the Toomre wavelength, defined as:

$$\lambda_c = \frac{4\pi^2 G\sigma}{\Omega^2}, \qquad (10)$$

where G is the gravitational constant and σ is the surface density. Previous simulations (Salo 1992; Daisaka & Ida 1999) have shown that the typical spacing of wakes is close to λ_{cr}.

For each simulation, we choose a single combination of particle density and particle radius (monodisperse distribution) that corresponds to a constant optical depth. This is done in order to ensure λ_c is kept constant across all simulations that use the same dynamical optical depth, allowing us to draw

more accurate comparisons of simulation outcomes across different particle density and cohesion cases. The main parameters for the simulations are summarized in Table 1.

Typical run times were between 0.3 and 40 kSU, where one SU is equal to 1 hr of wall clock time on a single core of a CPU, and 1000 SU = 1 kSU.

2.4. Diagnostics: Clump Finding Algorithm

In order to determine the effectiveness of cohesive forces to clumping particles together, we developed a procedure to measure the sizes of particle aggregates in the patch. While aggregates may easily be distinguished by the human eye, naiive computational procedures are often fooled by tenuous connections or overlaps that lead to overestimates of aggregate sizes. Our approach divides the patch into grid cells, calculates the projected particle number in each cell (particle number density), extends search branches from the highest-density cell, and checks along each branch to determine the aggregate semimajor axis, semiminor axis, ellipticity, and orientation. Since self-gravity tends to keep particles in the midplane, most of the aggregates formed can be analyzed as two-dimensional structures in the x–y plane. As a result, it is not necessary to analyze the aggregate size in 3D, which saves computational time. We use 20 radial branches for each search. For expediency and accuracy, the branches' extent is limited to one-fourth of the patch from the highest particle density cell. We found this to be sufficient since aggregates are smaller than one-fourth of the patch size; furthermore, coherent structures of the order of the patch size invalidate the assumptions of the sliding patch model. However, the clump-finding algorithm adopted here only uses the distribution of surface number density of particles and does not check if the identified aggregate is actually forming a shear-free structure or not.

Branches are drawn in 18° intervals for symmetry. Cells are sampled along each branch until the projected number of particles in the cell drops below a threshold fraction of the maximum central projected particle number. If a branch passes partly between two cells, the average particle number in each neighboring cell is used. The threshold fraction can be adjusted for different cases since low-cohesion simulations are more likely to form wakes instead of aggregates. For example, if a smaller threshold is used in low-cohesion analysis, the aggregate semimajor axis is likely to be identified as the whole vertical wake structure. Figure 1 shows results of the analysis using a threshold of 0.1 (left) compared to a threshold of 0.5
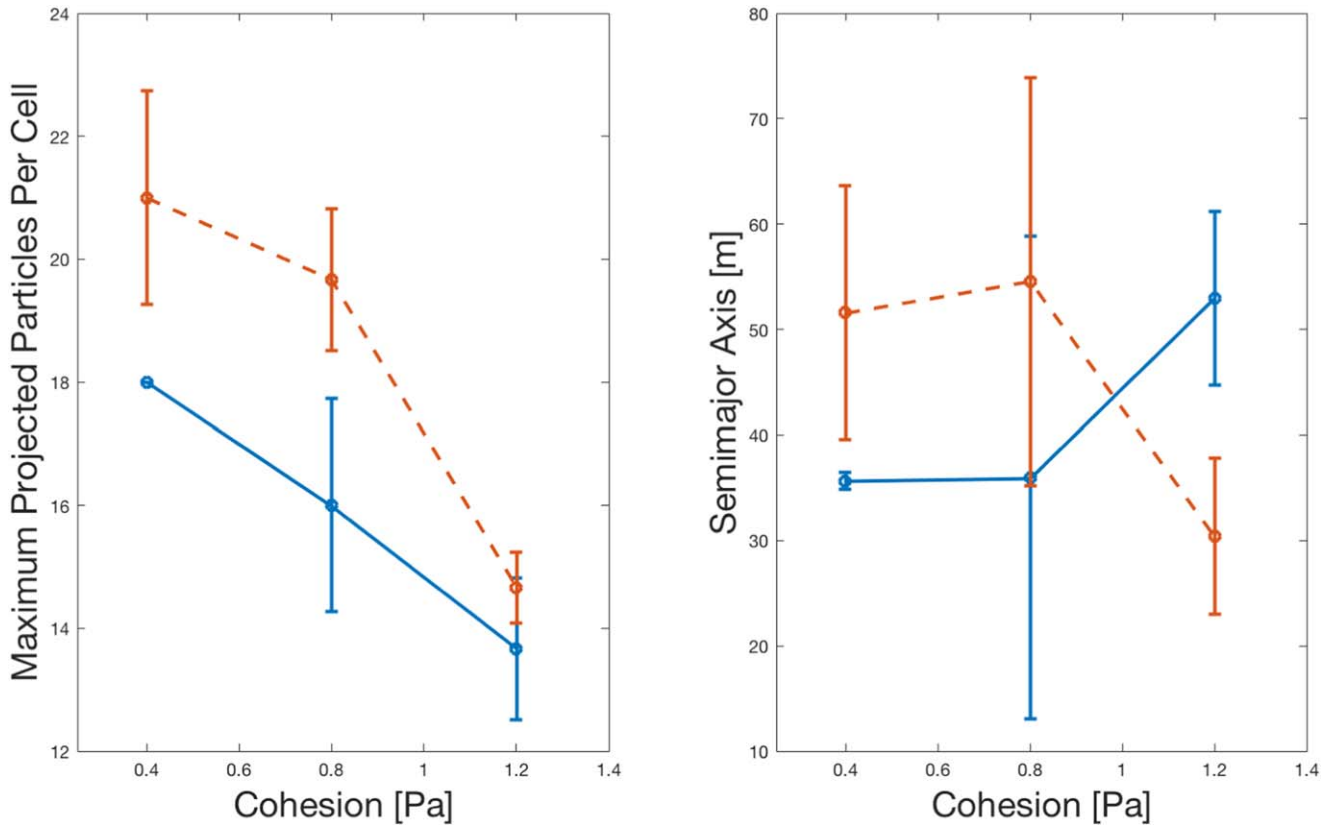
Figure 2. Maximum projected particle density and biggest aggregate semimajor axis, as determined using the clump-finding algorithm for two different patch sizes: $10 \times 10\lambda_c$ (blue solid line) and $4 \times 4\lambda_c$ (orange dashed line). Averages are formed by computing values from three different snapshots taken roughly three orbits apart after equilibrium is established. Error bars show the 1σ standard deviation. Three different cohesive strengths were analyzed for each patch size. The statistical differences between the results for the two patch sizes are small.

(right) for a cohesion value of 6.6×10^{-3} Pa. Because the particle per cell value decreases rather slowly along the gravity wake structures, instead of converging on an aggregate shape, the search continues along the wake. Ultimately, a threshold fraction value of 0.5 was chosen through trial and error based on visual inspection. The semimajor axis of the structure is then calculated as half of the maximum extent achieved along two oppositely oriented branches.

In order to ensure the algorithm is not sensitive to patch size, we performed the analysis for two different patch sizes, as shown in Figure 2. Three different snapshots taken over three orbits after equilibrium is established were used to perform the average. Error bars show the 1σ standard deviation. Three different cohesive strengths were analyzed for each patch size. For consistency, the three simulation time steps were chosen to be the same for both patch sizes. Since the results are fairly similar in each case for the two patch sizes, we conclude that the smaller patch size is sufficient for characterizing the results of these simulations.

3. Results

We performed 120 simulations over nine different cohesion values ranging from 5×10^{-2} to 7.0 Pa, dynamical optical depths (τ_{dyn}) of 0.8, 1.4, and 1.8, particle densities (ρ) of 0.5 as well as 1 g cm^{-3}, and restitution coefficients of 0.8 and 0.55 for both normal and tangential components.

Figures 3 and 4 show snapshots from our simulations, with square frames showing overhead views and narrow horizontal frames beneath each of these showing corresponding edge-on views. We distinguish two different equilibrium structure types as the cohesion is increased from low to high values (left to right in each group of snapshots). For low cohesion values, self-gravity wakes dominate. For high cohesion values, unexpectedly, the wake structure dissipates and the ring particles become uniformly distributed over the whole patch. Moreover, the edge-on views show an abrupt growth in the z velocity distribution as the wake structure dissipates. This sudden transition happens at slightly lower cohesion values for smaller restitution coefficients and seems to not be correlated with the particle bulk density (the top group of snapshots in the figure are for $\rho = 1$ g cm^{-3} while the bottom group are for 0.5 g cm^{-3}; within each group, the top row of snapshots are for $\tau_{dyn} = 0.8$, the middle row are for 1.2, and the bottom row are for 1.8). Some simulations stopped before the system reached equilibrium due to violation of periodic boundary that the model assumed at high cohesion that structures cannot extend too far across the patch. We marked these runs with red boxes in the figure in order to indicate that the analysis for these runs might not be accurate.

Analysis using the clump-finding algorithm is shown in Figure 5. We measure the mean of the largest clump size in a patch by performing the clump-finding calculation at three equally spaced phases of the final orbit of each simulation. The error bars

Particle Material Density 1 g*cm^-3 EpsN/EpsT=0.8
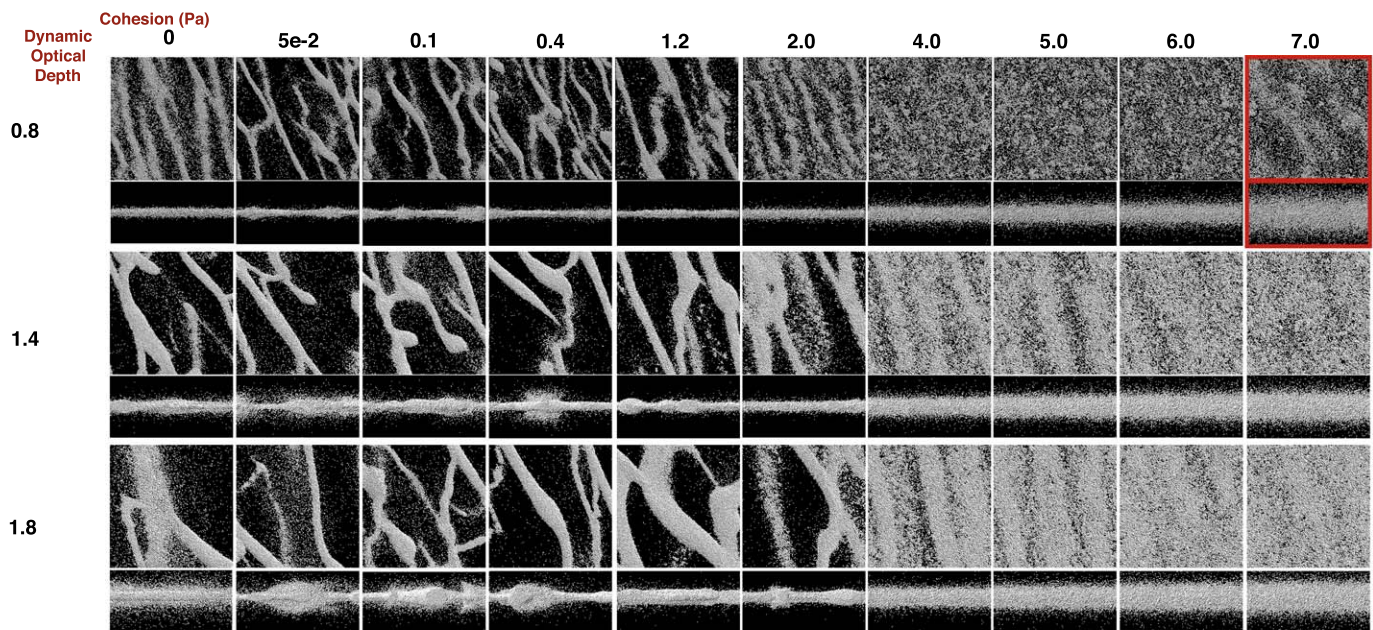
*Solid red box shows runs that has not reach equilibrium
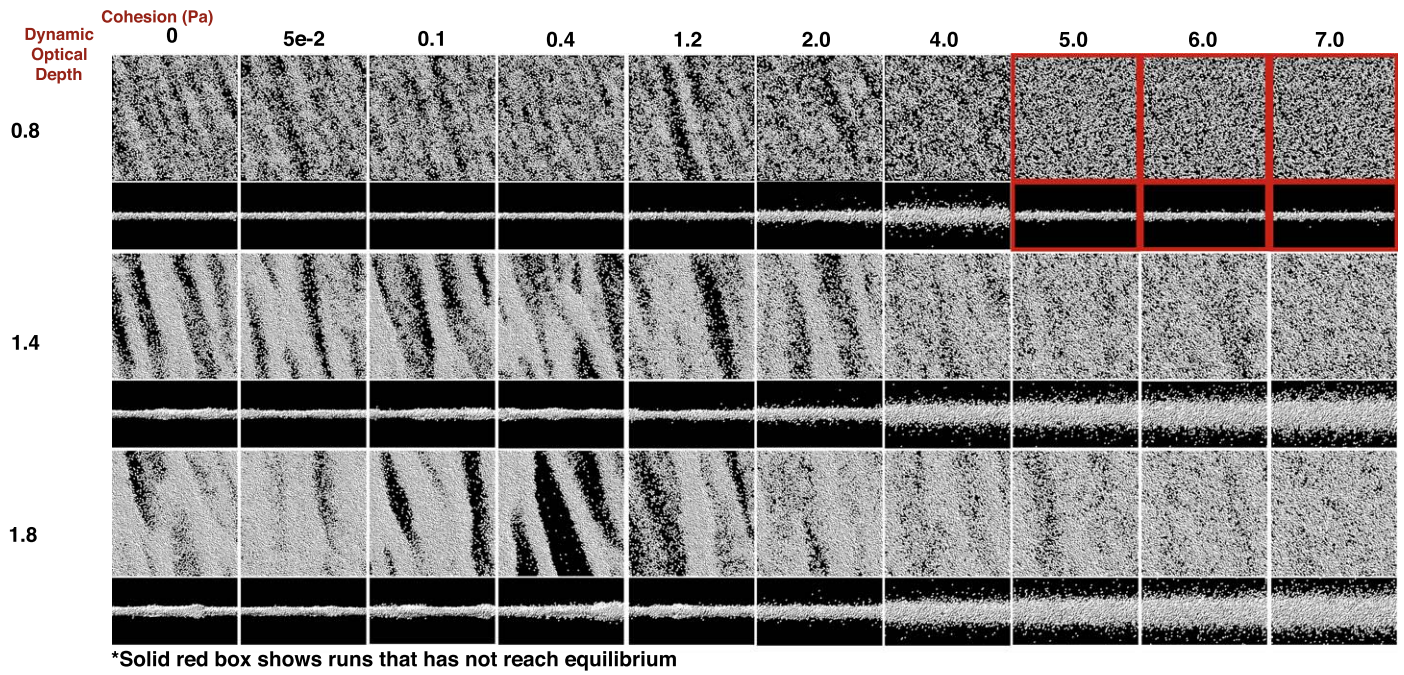
Particle Material Density 1 g*cm^-3 EpsN/EpsT=0.55
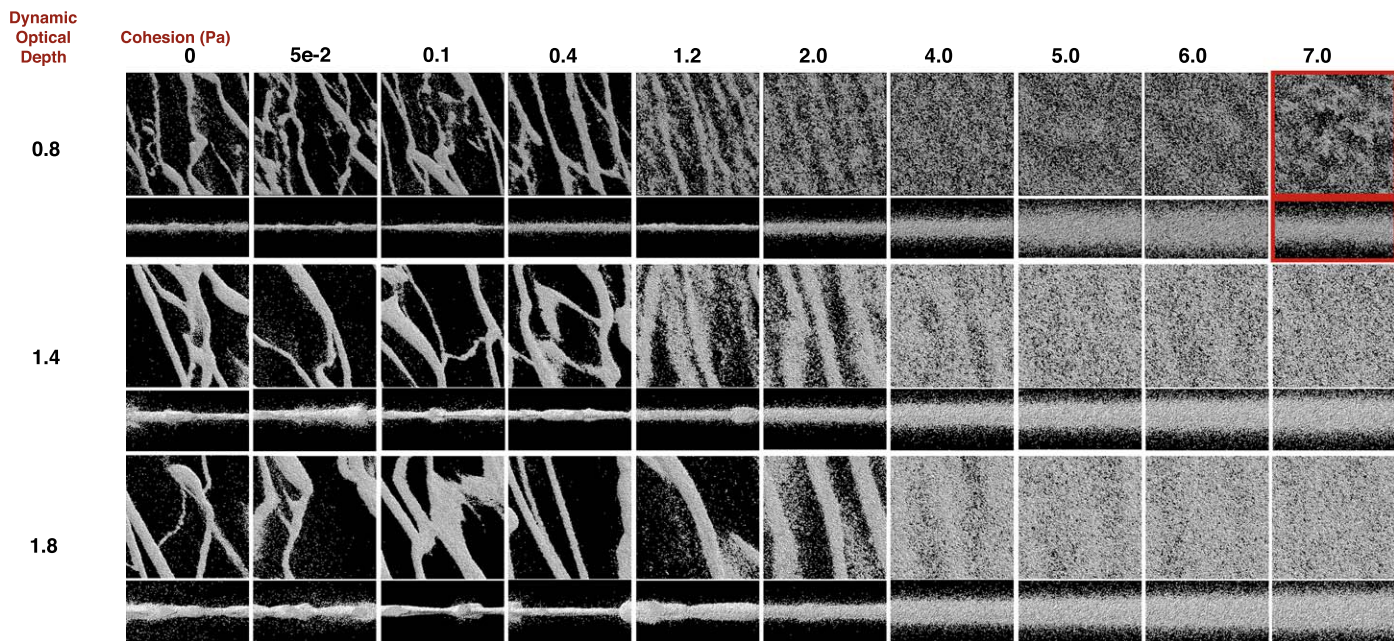
*Solid red box shows runs that has not reach equilibrium

Figure 3. Snapshots from the simulations for particle material density 1 g cm^{-3} (top) and 0.5 g cm^{-3} (bottom) for a lower energy dissipation rate at comparable times after equilibrium is achieved (except in the case of simulations with the highest cohesion values marked by red boxes, which were stopped early). Each snapshot consists of a top-down view of size $\sim$300 $\times$ 300 m for density 1 g cm^{-3} and $\sim$150 $\times$ 150 m for density 0.5 g cm^{-3} and a corresponding edge-on view underneath at the same scale.

shown represent the standard deviation of these three measurements. Results show that the aggregate semimajor axis as well as the maximum particle number density decreases with increasing cohesion. This is more obvious for the higher-density simulations compared to the lower-density simulations due to the more prominent self-gravity wake structure in higher-density simulations (see Figures 3 and 4). However, it is clear that the aggregate size decreases to near zero as the self-gravity wake structure

Particle Material Density 0.5 g*cm^-3 EpsN/EpsT=0.8

*Solid red box shows runs that has not reach equilibrium

Particle Material Density 0.5 g*cm^-3 EpsN/EpsT=0.55

*Solid red box shows runs that has not reach equilibrium
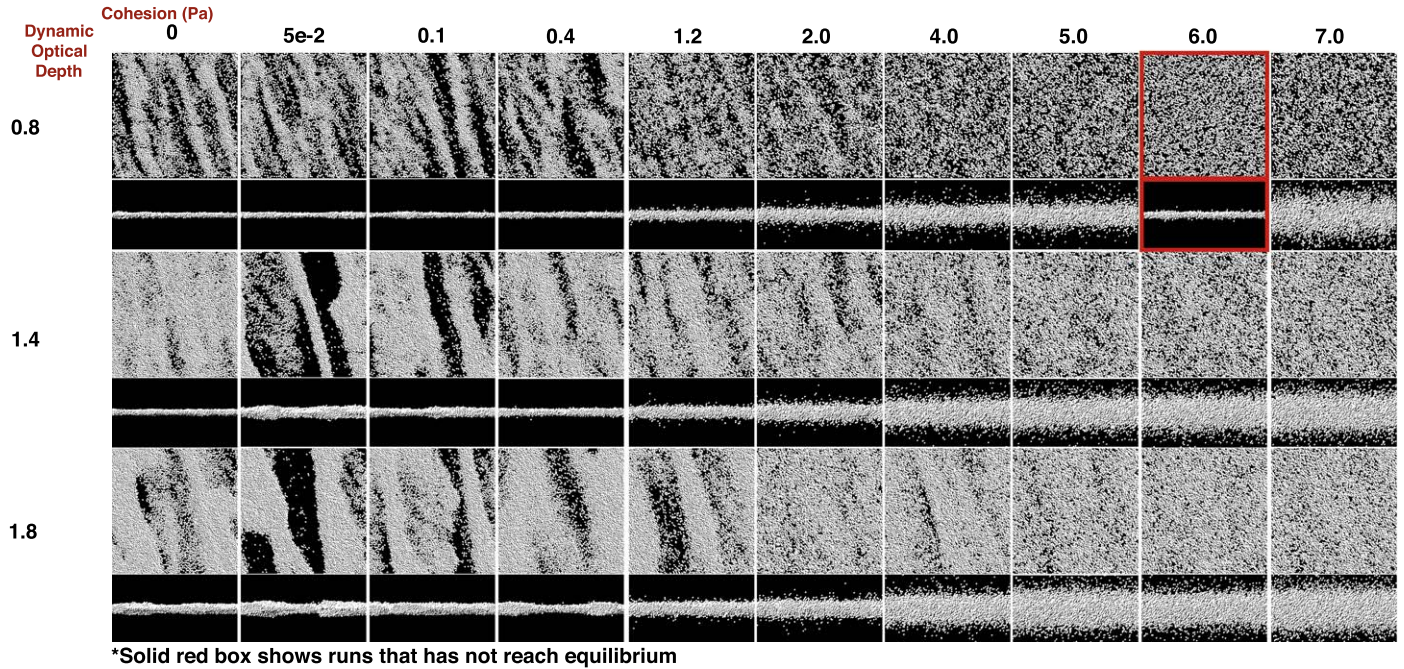
Figure 4. Same as Figure 3 but for a higher energy dissipation parameter.

disappears and the maximum particle number density reaches equilibrium at the same time.

We also calculated the physical optical depth (τ_{phy}) using a Monte Carlo ray-shooting simulation, where τ_{phy} is defined as

$$\tau_{phy} = -\ln f, \tag{11}$$

where f is the fraction of the rays that pass through the patch vertically without intersecting any ring particles. Figure 6 shows the result for our simulations. Evidently, the physical optical depth plateaus around the dynamical optical depth value when the abrupt transition happens (~ 2 Pa cohesive strength),
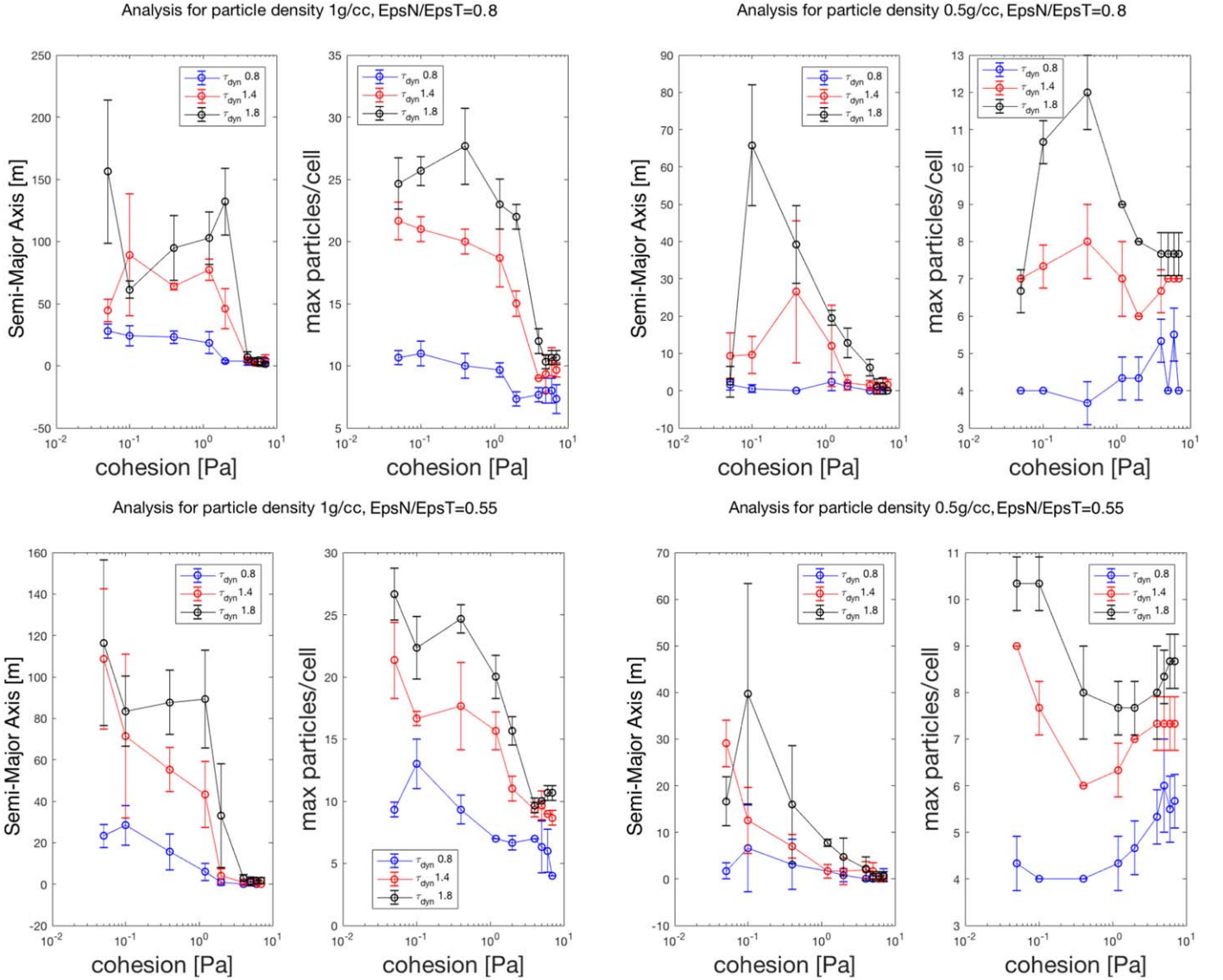
Figure 5. Analysis of the aggregate semimajor axis as well as the maximum particle density using the clump-finding algorithm. The values are obtained by taking the mean measured aggregate size at three equally spaced phases of the final simulated orbit, and the uncertainties represent the standard deviation of these three measurements.

and we find this happens when the particles become more uniformly distributed in the patch (so there is less clumping).

4. Discussion

4.1. Disaggregation and Disk Heating

We find that particles in Saturn's opaque rings have a nonintuitive relationship between their cohesive strengths and the maximum structure size that they can form. It was expected that ring particles were more likely to form aggregates as interparticle cohesion increases; however, we find that large values of cohesion frustrates aggregate growth, and self-gravity wake structure is destroyed. Furthermore, we find that this process tends to cause a sharp increase in the z velocity dispersion of the ring.

From visual comparisons of the early stages of a low-cohesion simulation and a high-cohesion simulation, as shown in Figure 7, we find a possible explanation. We observe that ring particles with high cohesion form large aggregates extending in the radial direction, and these aggregates are then rotated by the tidal shear, collide, and break apart, injecting a

massive amount of energy into the system. This may explain why the system has a "hotter" equilibrium state where the z velocity dispersion is high and no large aggregates are able to persist.

The evolution of the total kinetic energy per unit mass for low and high cohesion values further supports this hypothesis (Figure 8). This quantity is calculated by summing up the translational kinetic energy ($\frac{1}{2}mv^2$) and the rotational kinetic energy ($\frac{1}{2}I\omega^2$) from each particle and dividing by the total mass of the system. Here the moment of inertia $I = \frac{2}{5}mR^2$ for a spherical particle of mass m and radius R. The analysis shows a systematic difference between the high-cohesion run and the low-cohesion run at an early stage. With high cohesion, the system gained a huge amount of kinetic energy, presumably through tidal shearing as explained in the previous paragraph, near the start of the simulation. As the large aggregates are broken down by collisions, the energy injection slows down and the energy dissipation from collisions rapidly increases. This causes a rapid decrease in the total kinetic energy until an
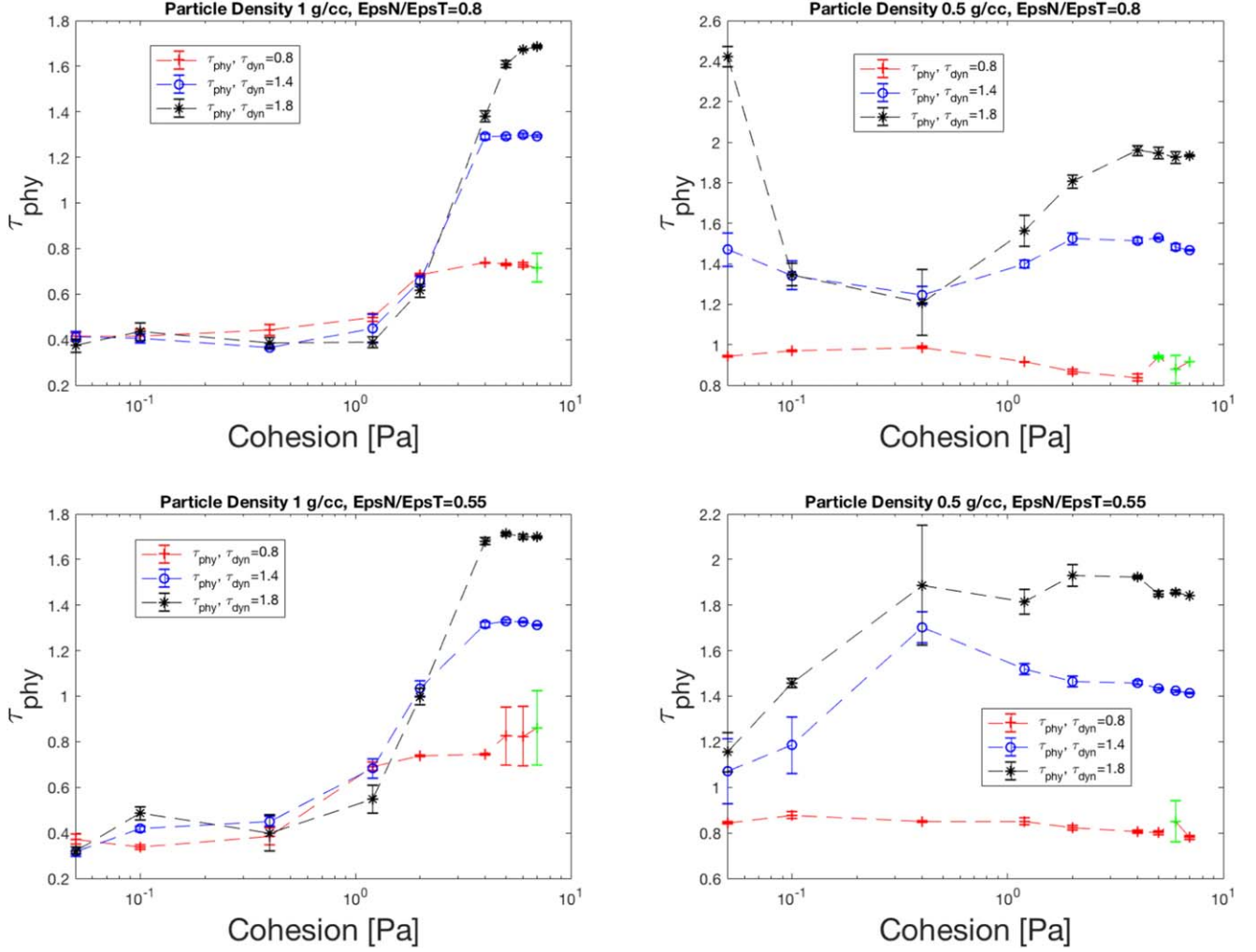
Figure 6. Physical optical depth (τ_{phy}) from Monte Carlo ray-shooting simulations for particle material density 1 g cm^{-3} (top/bottom left) and 0.5 g cm^{-3} (top/bottom right). Three calculations are performed on each of the simulations that has a nonzero cohesion value, except the ones that did not reach equilibrium (marked by the green markers). The mean values and standard deviations are shown. Note the differing vertical scales.

equilibrium state is reached, where the energy injection from tidal shear is balanced by the energy dissipation. Therefore, the system reaches a more uniform "hotter" equilibrium, compared to the low-cohesion case, which gradually gains energy from the tidal shearing before approaching a slightly lower equilibrium value compared to the high-cohesion case.

Visual inspection of the snapshots of the early stages of a simulation with high restitution coefficients compared to that of low restitution coefficients with the same cohesive strength reveals a negative relation between the radial structure size and the restitution coefficients (see Figure 9), since lower restitution coefficients correspond to a higher energy lost when particles collide, which potentially increases the structure size. Larger structures can carry more energy, and this could explain why simulations with low restitution coefficients result in an earlier transition from wakes to structureless form.

The hypothesis that bigger aggregates form with higher energy loss can also be confirmed by analyzing the particle speed distribution. We plotted the magnitude of the velocities (v) for all particles (see Figure 10) using $v = \sqrt{v_x^2 + v_{y_{\mathrm{noShear}}}^2 + v_z^2}$,

where v_x, $v_{y_{\mathrm{noShear}}}$, v_z are the particle velocity components in the x, y, z direction after subtracting the shear speed in the y direction. The result shows larger aggregates forming for the high-energy-loss runs at a cohesive strength value of 7 Pa. Although the boundary condition might have played a role in breaking up the particles due to their large radial extent, there are significant clumps undergoing high rotation well inside the patch. The same test also shows that low-cohesion runs at the same moment in time have no particles that have speeds greater than 0.5 cm s^{-1} or any large aggregates forming.

We also analyzed the radial velocity of particles (x direction). For rotating clumps, we will expect a smooth transition of x velocity from small to large as the particle distance from the center increases, which is what we see for the clumps identified in Figure 11 by the red circles. These two tests further support our hypothesis that shear-induced rotations of large clumps inject energy at high cohesion values.

The same test for velocity in the x direction is performed on a larger patch size ($10 \times 10\,\lambda_c$) in order to ensure the boundary condition is not the main factor in breaking up large aggregates. Figure 12 shows the aggregates in the same color scale shown
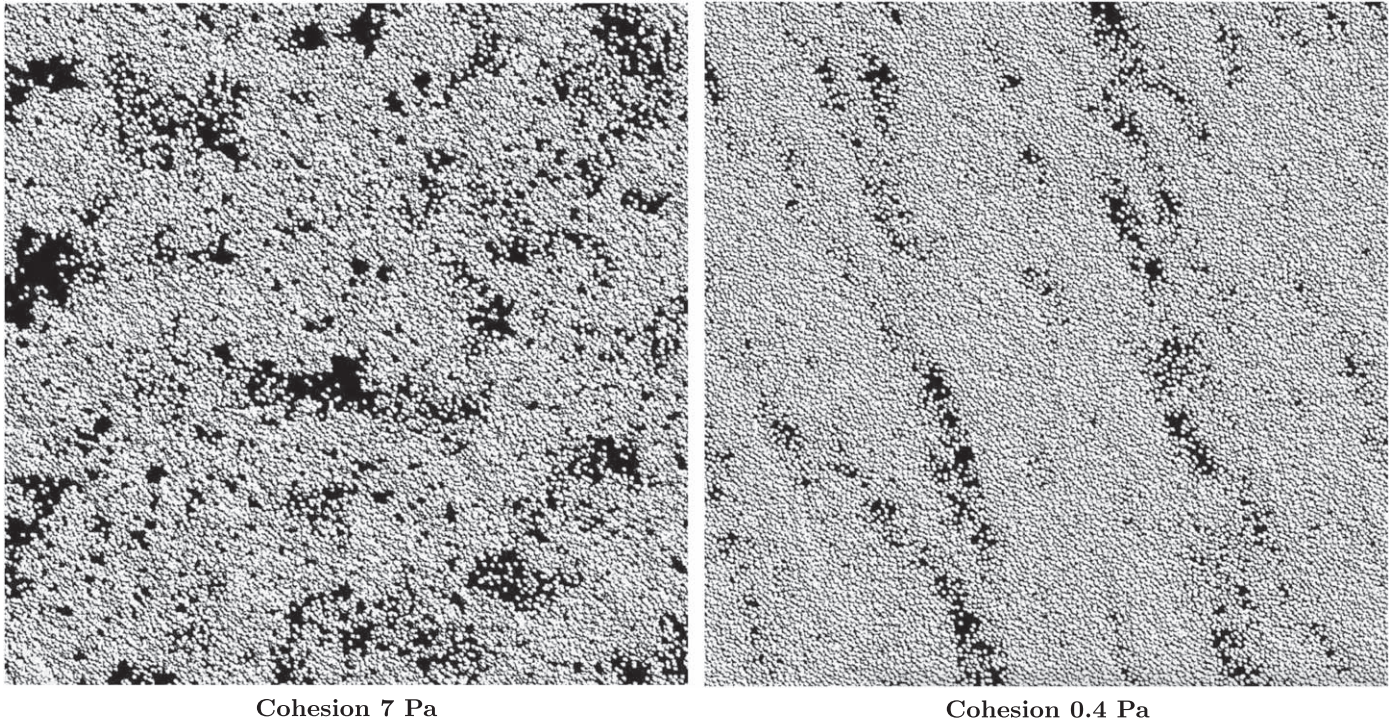
Particle Material Density 1 g cm^{-3}, $\varepsilon_N //\varepsilon_N$=0.8

Cohesion 7 Pa   Cohesion 0.4 Pa

Figure 7. Snapshots of the early stages of a high-cohesion simulation (left) and a low-cohesion simulation (right). It is evident that the structure forming at high cohesion extends more radially compared to that at low cohesion. This allows tidal shear to rotate the structure and inject energy into the system.

Total Kinetic Energy Per Unit Mass

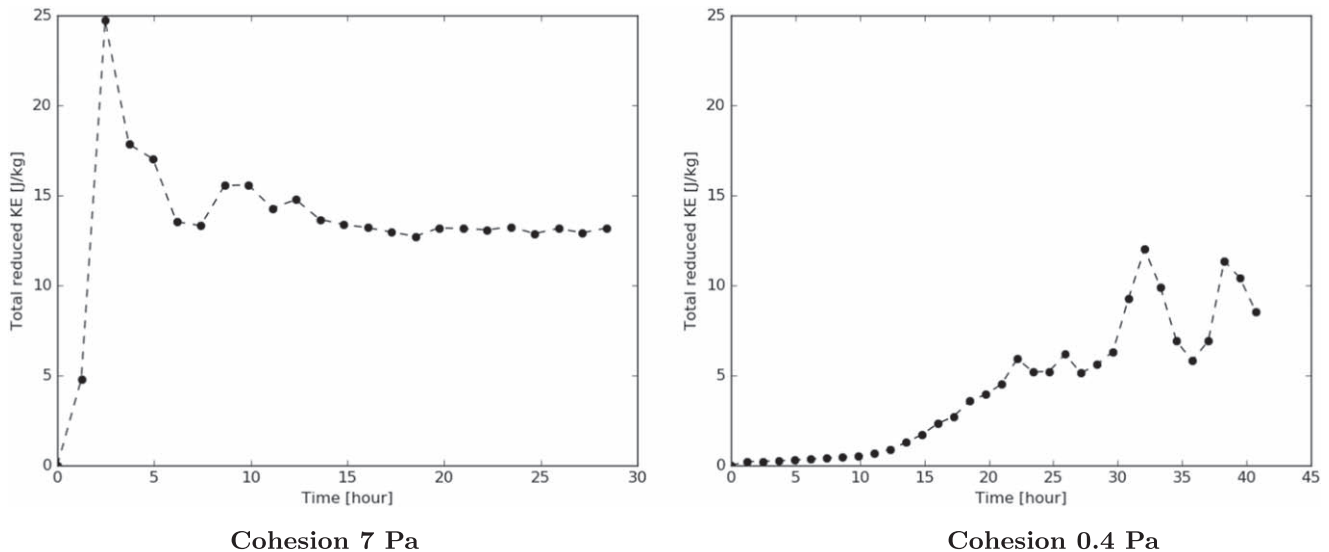Cohesion 7 Pa   Cohesion 0.4 Pa

Figure 8. Total kinetic energy (sum of translational and rotational) per unit mass of a high-cohesion and a low-cohesion simulation over three to four orbits.

in Figure 10. The red solid line carved out one of the aggregates. Compare to that of a smaller patch size, the difference in aggregate size is visually invisible.

If our explanation is correct, shear-free rings around Saturn might not be possible since any small perturbation could start a large aggregate rotating for sufficiently cohesive particles, resulting in high collision speeds and destruction of the aggregate.

4.2. Theoretical Limit of Structure Growth

While we have demonstrated that cohesion limits the growth of subkilometer structures ($\sim$100 m) in the B-ring, the analysis

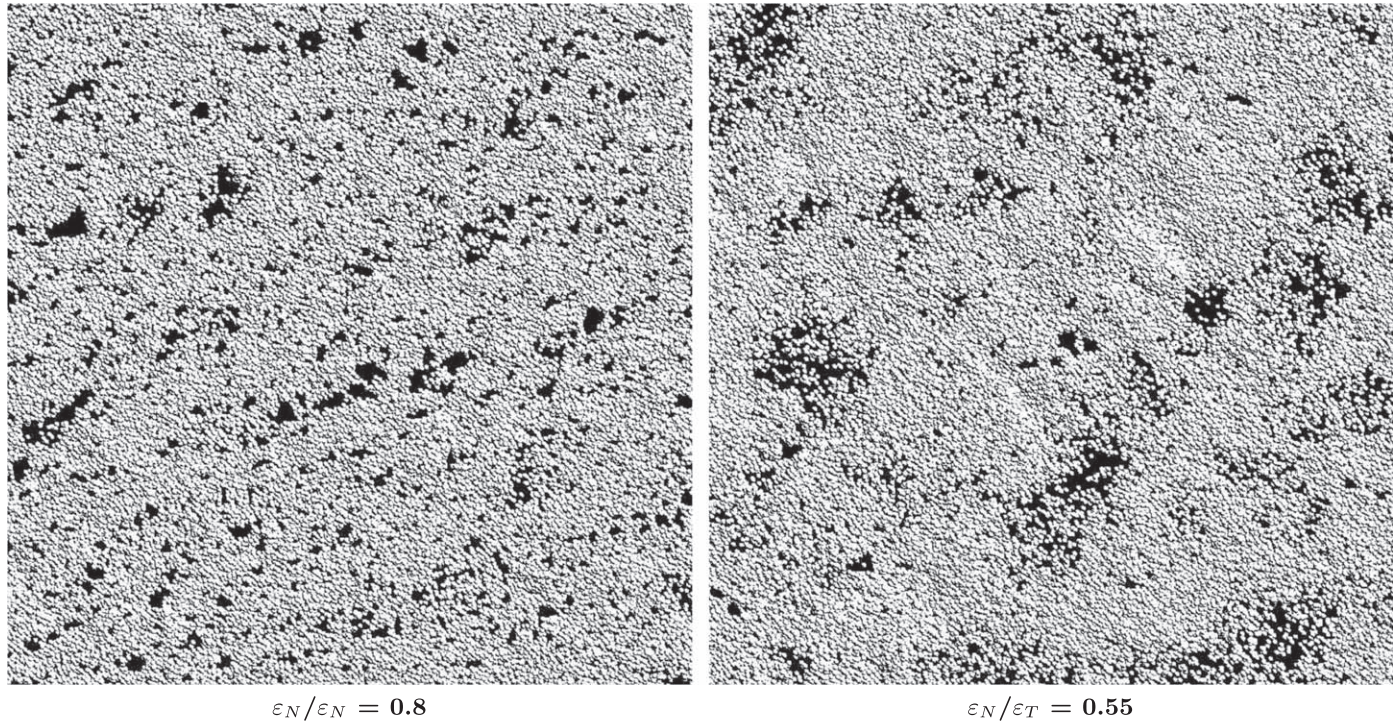Particle Material Density 1 g cm^{-3}, Cohesion 7 Pa

$$\varepsilon_N/\varepsilon_N = 0.8 \qquad\qquad\qquad \varepsilon_N/\varepsilon_T = 0.55$$

Figure 9. Snapshots of the early stage of simulations with high restitution coefficients (left) and low restitution coefficients (right). The radial structures forming with lower restitution coefficients are larger in size compared to the ones with higher restitution coefficients.
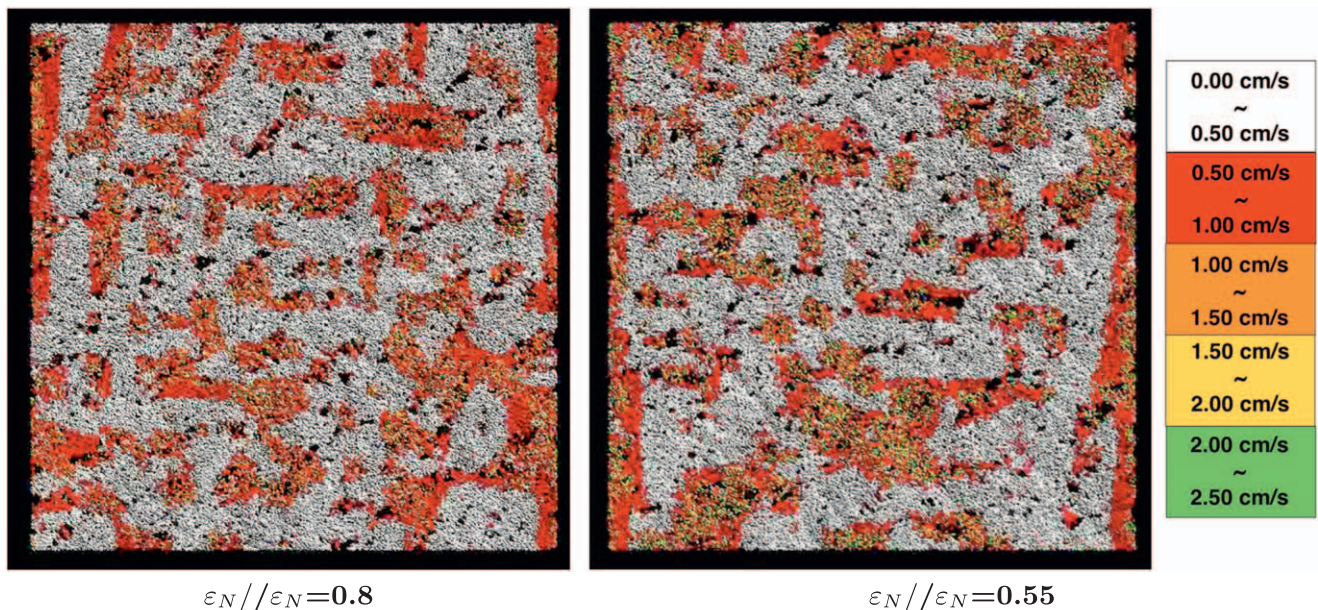
Particle Material Density 1 g cm^{-3}, cohesion coefficient 7 Pa

$$\varepsilon_N//\varepsilon_N = 0.8 \qquad\qquad\qquad \varepsilon_N//\varepsilon_N = 0.55$$

Figure 10. Snapshots of the early stages of a high-restitution-coefficient run (left) and a low-restitution-coefficient run (right) at the same moment in time colored based on the particle speed distribution. The color scale is shown on the right.

of Tremaine (2003) had suggested that annuli of "solid" rings up to 100 km in size may form through interparticle cohesion if the tensile strength of the material was large enough. Here, we analyze the results of our simulation in light of these previous theoretical provisions.

By considering the shear rate of a solid annulus in Saturn's ring, Tremaine (2003) analytically demonstrated that the maximum tensile stress, C, that could be withstood by a rotating slab of width, Δr, and bulk density, ρ, that is located in the B ring (i.e., 10^5 km from Saturn) can be given by

$$C = 4 \times 10^4 \left(\frac{\rho}{0.3 \text{ g cm}^{-3}}\right)\left(\frac{10^{10} \text{ cm}}{r}\right)^3\left(\frac{\Delta r}{100 \text{ km}}\right)^2 \text{ Pa.} \quad (12)$$

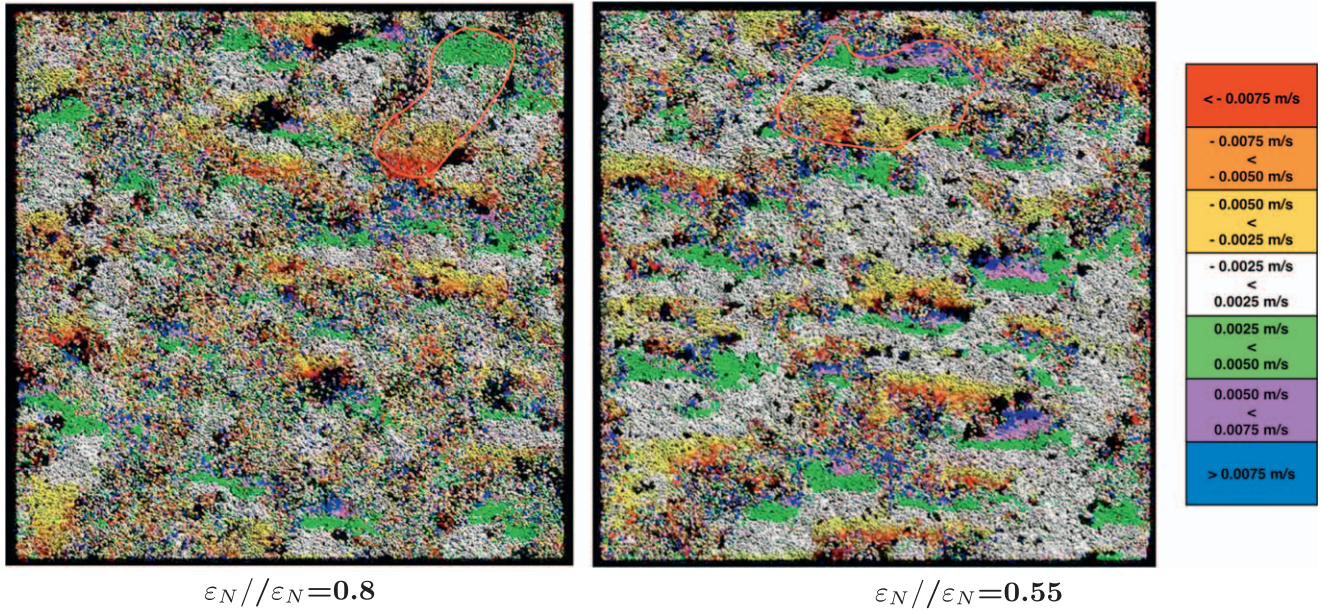## Particle Material Density 1 g cm^{-3}, cohesion coefficient 7 Pa

$\varepsilon_N//\varepsilon_N=0.8$ $\varepsilon_N//\varepsilon_N=0.55$

Figure 11. Snapshots of the early stages of a high-restitution-coefficient run (left) and a low-restitution-coefficient run (right) colored based on the particle x velocity distribution. The color scale is shown on the right and the red circles are clumps identified visually.
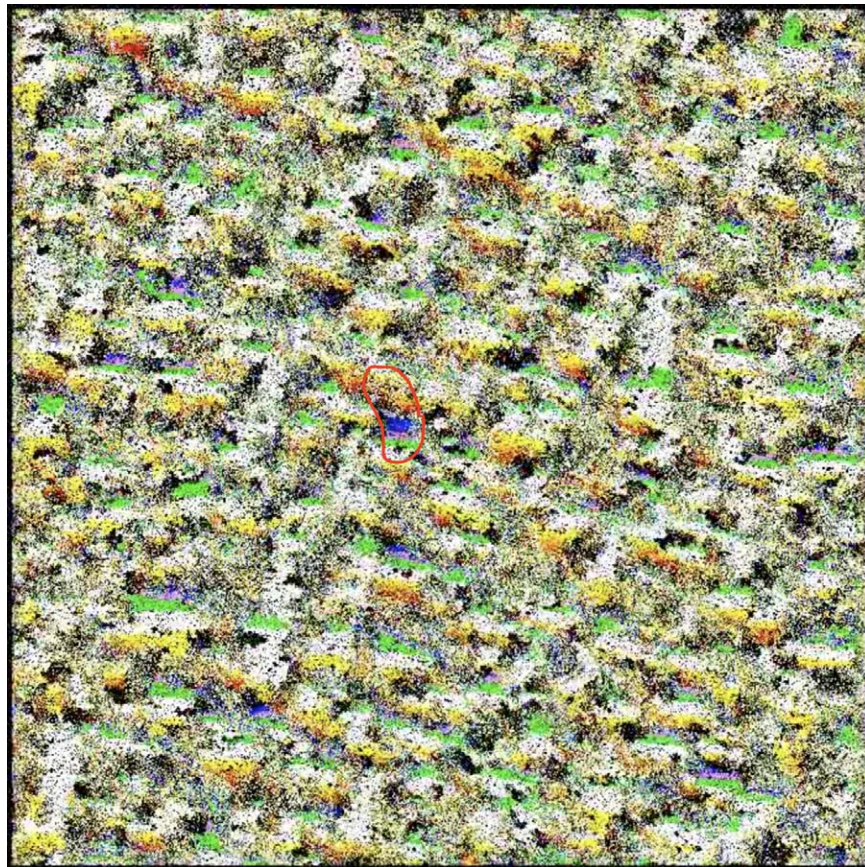

Figure 12. Snapshots of the early stages of a high-restitution-coefficient run for a larger patch size colored based on the particle x velocity distribution shown in Figure 10.

We can compare the results of our simulations to these theoretical expectations by equating C to the expected bulk tensile strengths that we simulated. Here, we note that the bulk tensile strength differs from the interparticle cohesive strength, c. It is difficult to determine a precise relationship between these two values as the bulk tensile strength of an aggregate
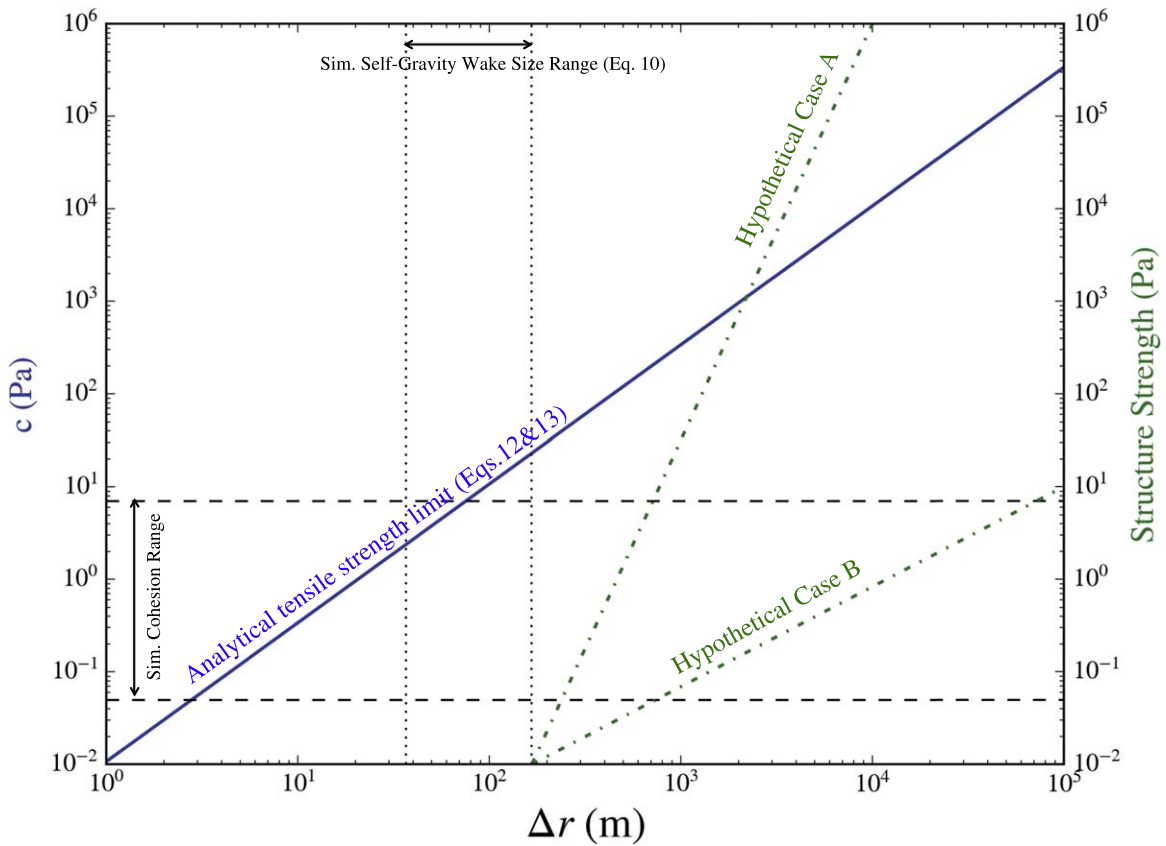
Figure 13. Maximum structure size, Δr, that can form for a given interparticle cohesive strength, c, as determined by Equations (12) and (13). The black dashed lines represent the range of c that we explored in this study. The black dotted lines represent the size range of self-gravity wakes modeled in our simulations. The formation of these wakes combined with cohesive aggregation leads to structures with sizes that are unstable against disaggregation. For the formation of stable structures, the tensile strength of an aggregate needs to grow with size at a sufficient rate (Hypothetical Case A). The turnover point for stable structures to exist occurs for the range of values where the green dashed–dotted curve lies above the blue solid curve. If experimental or simulation results can show that structure strength grows at a rate that is slower than the tensile stress limit (Hypothetical Case B), they demonstrate that shear-free rings cannot exist around Saturn.

will depend on the average number of grain interactions, grain properties such as shape and sizes, and the geometrical structure of the aggregate. Nevertheless, we estimate this relationship between c and C from simulations of spherical aggregate spin destabilization by Zhang et al. (2018), who demonstrate the following empirical relationship using the same cohesion model and friction parameters as those of this study,

$$c \simeq 120 \times C^{0.75}. \tag{13}$$

By equating Equations (12) and (13), we evaluate the necessary interparticle cohesive strength for a given Δr, for a structure bulk density of $0.3\,\mathrm{g\,cm^{-3}}$ (Figure 13).

We find that for the range of interparticle cohesion we explored here (black dashed lines), the theoretical maximum structure size ranges from approximately a few to 100 m in size. However, the analysis does not account for the formation of self-gravity wakes that create large-scale structure without the aid of cohesion. The typical sizes of these wakes are set by the ring surface density, given by Equation (10). If self-gravity is considered, as was done in our simulations, then the cohesion acts to create structures that are larger than wake structure, which will require tensile strengths that exceeded the limit set by Equation (12) (solid blue line) for stability. Therefore, it is likely that the combination of self-gravity and cohesion that leads to the unstable growth of structure. Nevertheless, there may be some conditions in which cohesion may build stable large-scale structures. The green dashed–dotted

curves in Figure 13 represent two hypothetical scenarios for the growth of the structure strength with size for the case of a ring that starts with self-gravity wakes that are a few 100 m in size. For Case A, increases in structure size lead to growth in structure strengths that exceed the estimated growth given by Equation (12), while Case B represents a shallower growth in structure strength in size. If real ring particles can create structures that behave like Case A, then "solid" ring annuli should exist above a certain size (intersection between blue and green curve). For structure strength growth as represented by Case B, a solid ring will always be unstable against shear deformation, regardless of size. Measuring the dependence of structure strength with size and interparticle cohesive strength is beyond the scope of this study; however, this analysis provides a baseline for future theoretical investigations for large-scale structure stability through grain cohesion.

5. Conclusions and Future Work

Here we presented a study of the effect of interparticle cohesion in numerical simulations of Saturn's opaque rings. We used a highly optimized N-body code, pkdgrav, that models particle self-gravity, soft-sphere collisions, and interparticle cohesion to simulate a patch of Saturn's rings with periodic boundaries. Simulations from 120 runs, including nine different cohesion values ranging from 5.0×10^{-2} to $7.0\,\mathrm{Pa}$, dynamical optical depths of 0.8, 1.4, and 1.8, particle material densities of 0.5 and $1\,\mathrm{g\,cm^{-3}}$, and restitution coefficients of 0.8 and 0.55, show that gravitational wakes are suppressed at around $2\,\mathrm{Pa}$. This

transition seems to happen at lower cohesion for higher energy dissipation but shows no correlation with the particle material density. Our results show that particle aggregation leads to the formation of large clumps that do not have a preferred orientation in the ring plane. As these aggregates grow in length in the radial direction, they are spun-up by the tidal shear, injecting a massive amount of energy into the system and breaking up the aggregates. Therefore, the differential shear of the rings effectively limits the size of aggregates that are able to form in the opaque rings, for the range of cohesion values explored here. This process of particle clumping and subsequent disruption leads to the system having a dynamically hotter equilibrium state, where the z velocity dispersion is high and no large structures are able to form. These simulations suggest that small perturbations could frustrate the formation of shear-free zones of "solid" material in the rings.

Furthermore, we find that high values of interparticle cohesion limits the formation of subkilometer viscous overstability structures and self-gravity wakes (Ballouz et al. 2017; Lehmann et al. 2017), that have been verified through *Cassini* observations (Hedman et al. 2014). For viscous overstability structures to form, ring particles need to be focused into the ring midplane. As we have demonstrated, for a certain value of interparticle cohesion, large clumps of particles tend to disaggregate, injecting energy into the system and increasing the scale height of the ring. This leads to a tendency for the ring to homogenize rather than forming the optical depth structure we observe today. Therefore, we conclude that the expected interparticle cohesion in Saturn's ring particles today is fairly low (<2 Pa), for the material properties assumed in this study, and cohesion, as modeled in this study, may not have a dominant role in particle collisional dynamics. The frictional and dissipation properties of ring particles have been attempted to be inferred through comparisons of numerical simulations Ballouz et al. (2017) and observations Morishima et al. (2016); however, they are still poorly constrained. Furthermore, the relative cohesive strengths of particles are highly influenced by the shape and structures (Morishima et al. 2017) of individual ring particles as it is sensitive to the contact area between particles. Therefore, future work should feed into showing the sensitivity of these findings to particle shape and dissipation properties to better constrain the upper limit of ring particle cohesion.

Finally, the manner in which we modeled interparticle cohesion in this study is through invoking a "granular-bridge" model (Sánchez & Scheeres 2014; Zhang et al. 2018), where only the bulk cohesive effect of small grains on the surface of ring particles is modeled, rather than having an actual particle size distribution. While the ring particles in our simulation are all 1 m in radius, observational analysis by Becker et al. (2016) suggests that the minimum grain size in Saturn's A ring is ∼1 mm. The theoretical formulation of shear-free zones as presented in Tremaine (2003) was through the small particles acting as "glue" for large particles together, and the resulting predicted cohesive strengths were for structure sizes that were orders of magnitude larger than those explored in this work. Therefore, future work will focus on studying what the effect of an actual size distribution of particles would have on structure formation. Another potential future study might consider starting with a "warmer" initial condition in which particles are given more random energy and a larger vertical dispersion to determine whether this additional energy suppresses early aggregate formation, resulting in a different final outcome than that found here.

ORCID iDs

Yuxi Lu (iD) https://orcid.org/0000-0003-4769-3273
Ronald-Louis Ballouz (iD) https://orcid.org/0000-0002-1772-1934
Derek C. Richardson (iD) https://orcid.org/0000-0002-0054-6850

References

Ai, J., Chen, J.-F., Rotter, J., & Ooi, J. 2011, Powder Technology, 206, 269
Albers, N., & Spahn, F. 2006, Icar, 181, 292
Ballouz, R.-L., Richardson, D. C., Michel, P., & Schwartz, S. R. 2014, ApJ, 789, 158
Ballouz, R.-L., Richardson, D. C., Michel, P., Schwartz, S. R., & Yu, Y. 2015, P&SS, 107, 29
Ballouz, R.-L., Richardson, D. C., & Morishima, R. 2017, AJ, 153, 146
Becker, T. M., Colwell, J. E., Esposito, L. W., & Bratcher, A. D. 2016, Icar, 279, 20
Bridges, F. G., Hatzes, A., & Lin, D. N. C. 1984, Natur, 309, 333
Brilliantov, N. V., Spahn, F., Hertzsch, J.-M., & Pöschel, T. 1996, PhRvE, 53, 5382
Colwell, J. E., Cooney, J. H., Esposito, L. W., & Sremčević, M. 2009, Icar, 200, 574
Colwell, J. E., Esposito, L. W., Sremčević, M., Stewart, G. R., & McClintock, W. E. 2007, Icar, 190, 127
Daisaka, H., & Ida, S. 1999, EP&S, 51, 1195
Hatzes, A. P., Bridges, F., Lin, D. N. C., & Sachtjen, S. 1991, Icar, 89, 113
Hedman, M. M., & Nicholson, P. D. 2016, Icar, 279, 109
Hedman, M. M., Nicholson, P. D., & Salo, H. 2014, AJ, 148, 15
Hill, G. W. 1878, AmJM, 1, 5
Iwashita, K., & Oda, M. 1998, Journal of Engineering Mechanics, 124, 285
Jiang, M., Shen, Z., & Wang, J. 2015, Computers and Geotechnics, 65, 147
Johnson, K. L., Kendall, K., & Roberts, A. D. 1971, RSPSA, 324, 301
Lehmann, M., Schmidt, J., & Salo, H. 2017, ApJ, 851, 125
Maurel, C., Ballouz, R.-L., Richardson, D. C., Michel, P., & Schwartz, S. R. 2017, MNRAS, 464, 2866
Mohamed, A., & Gutierrez, M. 2010, Granular Matter, 12, 527
Morishima, R., Spilker, L., Brooks, S., Deau, E., & Pilorz, S. 2016, Icar, 279, 2
Morishima, R., Turner, N., & Spilker, L. 2017, Icar, 295, 74
Perrine, R. P., & Richardson, D. C. 2012, Icar, 219, 515
Perrine, R. P., Richardson, D. C., & Scheeres, D. J. 2011, Icar, 212, 719
Porco, C. C., Baker, E., Barbara, J., et al. 2005, Sci, 307, 1226
Rein, H., & Latter, H. N. 2013, MNRAS, 431, 145
Richardson, D. C., Quinn, T., Stadel, J., & Lake, G. 2000, Icar, 143, 45
Salo, H. 1992, Natur, 359, 619
Salo, H., Schmidt, J., & Spahn, F. 2001, Icar, 153, 295
Sánchez, P., & Scheeres, D. J. 2014, M&PS, 49, 788
Scheeres, D. J., Hartzell, C. M., Sánchez, P., & Swift, M. 2010, Icar, 210, 968
Schmidt, J., Salo, H., Spahn, F., & Petzschmann, O. 2001, Icar, 153, 316
Schwartz, S., Richardson, D., & Michel, P. 2012, Granul. Matter, 14, 363
Schwartz, S. R., Michel, P., Richardson, D. C., & Yano, H. 2014, P&SS, 103, 174
Spahn, F., Albers, N., Sremcevic, M., & Thornton, C. 2004, EL, 67, 545
Stadel, J. G. 2001, PhD Thesis, Univ. Washington
Tremaine, S. 2003, AJ, 125, 894
Wisdom, J., & Tremaine, S. 1988, AJ, 95, 925
Yu, Y., Richardson, D. C., Michel, P., Schwartz, S. R., & Ballouz, R.-L. 2014, Icar, 242, 82
Zhang, Y., Richardson, D. C., Barnouin, O. S., et al. 2017, Icar, 294, 98
Zhang, Y., Richardson, D. C., Barnouin, O. S., et al. 2018, ApJ, 857, 15